Artificial Intelligence in Geosciences 5 (2024) 100070

Contents lists available at ScienceDirect

Artificial Intelligence in Geosciences

journal homepage: www.keaipublishing.com/en/journals/artificial-intelligence-in-geosciences

# Reservoir evaluation using petrophysics informed machine learning: A case study

Rongbo Shao [a,c], Hua Wang [a,b], Lizhi Xiao [a,c,*]

[a] College of Artificial Intelligence, China University of Petroleum, Beijing, 102249, PR China
[b] School of Resources and Environment, University of Electronic Science and Technology of China, Chengdu, 611731, PR China
[c] National Key Laboratory of Petroleum Resources and Engineering, China University of Petroleum, Beijing, 102249, PR China

ARTICLE INFO

*Keywords:*
Machine learning
Reservoir parameters evaluation
Data-mechanism-driven
Well logs

ABSTRACT

We propose a novel machine learning approach to improve the formation evaluation from logs by integrating petrophysical information with neural networks using a loss function. The petrophysical information can either be specific logging response equations or abstract relationships between logging data and reservoir parameters. We compare our method's performances using two datasets and evaluate the influences of multi-task learning, model structure, transfer learning, and petrophysics informed machine learning (PIML). Our experiments demonstrate that PIML significantly enhances the performance of formation evaluation, and the structure of residual neural network is optimal for incorporating petrophysical constraints. Moreover, PIML is less sensitive to noise. These findings indicate that it is crucial to integrate data-driven machine learning with petrophysical mechanism for the application of artificial intelligence in oil and gas exploration.

## 1. Introduction

Geophysical logging is a crucial tool for understanding subsurface resources. However, the traditional interpretation of logs based on petrophysical mechanism can be subjective and inefficient, often simplifying the petrophysical model in practice, which fails to accurately characterize complex reservoirs. Recent advancements in machine learning, big data, and high-performance computation provide new opportunities for data-driven logging interpretation. Bergen et al. (2019) are optimistic about the application of artificial intelligence in solid earth geoscience and its potential for analyzing large datasets, inverse theory, and computationally intensive simulations. Geophysical logs possess the characteristics of large data quantity and fast data updating, making them an ideal environment for data-driven machine learning method in logging interpretation.

In general, machine learning methods are commonly use for logs' interpretations in two domains: classification of lithology and the evaluation of reservoir parameters (Wang and Zhang, 2021). In the lithology classification, Adoghe et al. (2011) used principal component analysis (PCA) and self-organizing mapping (SOM) to predict electrofacies. Their experiments showed that SOM can effectively improve prediction accuracy. Jaikla et al. (2019) proposed a FaciesNet model, which combined convolutional autoencoders with bi-directional recursive neural networks to analyze lithofacies and the geological correlation of stacking patterns, while extracting geological information. They applied this model to predict geologically significant lithofacies from logs. Liu et al. (2020) suggested a lithofacies classification method based on the local deep multi-kernel learning support vector machine (LDMKL-SVM), which can simultaneously consider low-dimensional global features and high-dimensional local features. LDMKL-SVM could automatically learn the parameters of kernel function and SVM and establish the relationship between lithofacies and seismic elastic information.

In the evaluation of reservoir parameters, machine learning has demonstrated immense potential. Lee and Dattagupta (1999) proposed a two-step approach for permeability prediction that involved non-parametric regression and multivariate statistical analysis. Firstly, electrofacies are predicted from logs, and permeability models are constructed by alternating conditional expectations (ACE), generalized additive model (GAM), and neural networks (NNET) based on the electrofacie types. Lacentre and Carrica (2003) partitioned each reservoir region according to petrophysical information, and used neural networks and reservoir region restrictions to construct permeability models. Abdulraheem et al. (2007) presented fuzzy logic modeling to

* Corresponding author. College of Artificial Intelligence, China University of Petroleum, Beijing, 102249, PR China.
*E-mail address:* xiaolizhi@cup.edu.cn (L. Xiao).

https://doi.org/10.1016/j.aiig.2024.100070
Received 5 May 2023; Received in revised form 30 November 2023; Accepted 23 January 2024
Available online 24 January 2024

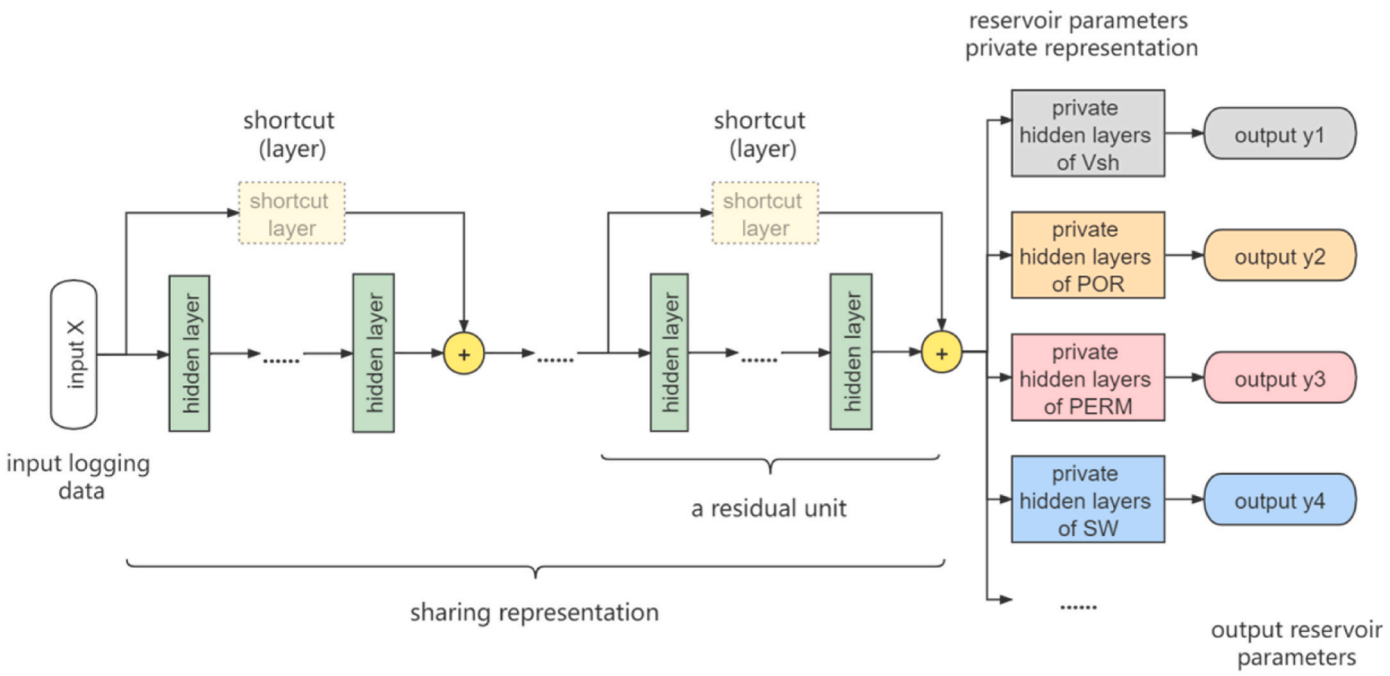


**Fig. 1.** Structure of multi-task residual neural network for reservoir parameters prediction.

predict permeability using logs, and the results are in good agreement with the core analysis. Male et al. (2020) used both machine learning and physics-based methods for permeability modeling of core data from 12 wells in the Garn Sandstone from the North Sea. The results showed that the machine learning method was superior to the physics-based method. Multi-task reservoir parameters modeling has also been proposed to simplify the process and make full use of the correlation between reservoir parameters. For example, Shao et al. (2022) proposed a multi-task neural network model to predicate reservoir parameters from logs that outperformed single-task models. They also analyzed the influence of multi-task learning models with various structures on the prediction effect of reservoir parameters and found that the prediction performance of different structure multi-task model was much better than other structures. As researchers continue to explore machine learning for logs' interpretation, they are gradually moving away from simple testing of existing machine learning models to constructing models that better fit the characteristics of logs, and to fusing multiple models to enhance performance.

In the application of data-driven machine learning in geophysics, various challenges limit further development, including interpretability (Chen and Wang, 2022), mechanism consistency, data complexity and uncertainty, small sample sizes, and few labels. Traditional formation evaluation models use mathematical and physical knowledge to explore input-output relationships, making it difficult to extract knowledge directly from data. Data-driven models extract knowledge from large datasets, but their quality depends on data quality, and their accuracy cannot surpass that of the data labels.

Since both mechanism and data-driven models have limitations in geophysical applications, the integration of data-driven machine learning and mechanism models has become a promising research direction in the field of geophysics. However, there are still many challenges to overcome. One of the major challenges is the selection of appropriate physical models that can effectively guide the data-driven models. Another challenge is how to combine the physical models with the data-driven models in a way that can balance the accuracy and interpretability of the results. Despite these challenges, many researchers have made significant progress in developing novel methods for fusing mechanism models and machine learning in geoscience. For example, Karpatne et al. (2017a) proposed theory-guided data science (TGDS), which leverages scientific knowledge to improve the effectiveness of data science models. Based on this, Karpatne et al. (2017b) developed a theory-guided neural network model (TGNN) to predicate lake temperature, which incorporates physical constraints into the loss function. Raissi and Karniadakis (2018) proposed a physical informed neural network (PINN) to solve partial differential equations (PDEs), which incorporates physical laws about general nonlinear PDEs into the loss function and trained the neural network model (Raissi et al., 2019). Kharazmi et al. (2019, 2021) extended the PINN to the Variational PINN (VPINN) by integrating the weak-form loss function into a fully connected neural network, which has high accuracy in solving high-order derivative problems and can compute integrals in sub-domains. In the oil/gas industry, many researchers explored the fusion of mechanism model and machine learning. For instance, Zhu and Zabaras (2018) proposed a Bayesian convolutional encoder-decoder deep network for uncertainty quantification tasks to solve the groundwater flow problem. (Wang et al. 2020a, 2020b, Wang and Zhang, 2021) applied the TGNN to solve groundwater flow problems and achieved higher accuracy than the DNN model, especially for processing complex and noisy data. Xu et al. (2021) proposed the weak form theory-guided neural network (TGNN-wf) for single-phase and two-phase underground flow, which archived higher accuracy, faster training, and more robust to noise than the TGNN model. Chen and Zhang (2020) proposed a physics-constrained indirect supervised learning method for generating logs. They (Chen and Zhang, 2021) further proposed a theoretical-guided deep learning for electrical load forecasting (TgDLF), which archived higher accuracy and better robustness and noise resistance than the LSTM model. Chen et al. (2021) proposed the theoretical-guided hard constraint projection (HCP) method. The model transforms physical constraints into a form that is easy to be discretized and then realizes hard constraint optimization through patch projection. Experiments showed that the hard constraint model was more robust than the soft constraint model, and theory had a stronger influence on the model. Wang et al. (2023) employ the SHAP method to assess the interpretability of four ensemble learning techniques in wave slowness prediction. Based on the experimental results, they observe that the mapping relationships identified by the machine learning models align with the physical principles of borehole acoustics. Recently, Xiao (2022) reviewed the research development on oil and gas artificial intelligence

and proposed that data-driven and mechanism model fusion modeling is an important breach to solve the application problems of industrial oil and gas artificial intelligence.

In summary, the fusion of data-driven machine learning and mechanism models has great potential in solvingcomplex problems in geophysics. Although there are still challenges to overcome, researchers have made significant progress in developing novel methods for integrating physical models and machine learning, and there is still much room for further exploration and development in this field.

In this study, we propose to fuse the petrophysical knowledge into the data-driven model by a loss function to constrain the training of the data-driven model with the mechanism model.

## 2. Principle of the method

The neural network model is one of the most representative data-driven machine learning, which has shown great potential in processing geophysical logs. In this study, we propose a novel method that leverages the neural network model as the basic model, and fuse the loss function and mathematically transformed petrophysical information to affect the training of the neural network. This section provides details in the explanation of the petrophysical informed machine learning method, including the construction of loss function, the classification of petrophysical information, and the structure of residual neural network model.

### 2.1. The residual neural network

The residual neural network, proposed by He et al. (2016) for the image classification, won the champion in the 2015 ILSVRC (Imagenet Large Scale Visual Recognition Challenge). It has been widely used in the field of machine vision due to its ability to solve the problem of gradient disappearance in deep learning. In logging parameters' prediction, logs contain a large amount of information, but their redundancy is much lower than that of image data, making information loss more likely to occur during the forward propagation of the neural network. The introduction of the residual neural network can fully retain the information of the previous layer and prevent the loss of effective information.

Fig. 1 shows the multi-task residual neural network for reservoir parameter prediction. The model is divided into sharing representation and private representation for reservoir parameters. The sharing representation extracts information related to reservoir parameter prediction from logging data, while the private representation is specific to each reservoir parameter prediction task. Each reservoir parameter prediction task needs to pass through the sharing representation in the forward propagation and participate in model parameters update in the back propagation. During forward propagating, the private representation only participates in the calculation of the corresponding reservoir parameter, while during back propagating, the private representation parameters are updated only under the influence of the reservoir parameter.

The residual structure exists in the sharing representation, connecting the output of the preceding layer with the input of the subsequent layer through a shortcut layer, which can adjust the size of the preceding layer output.

The operation process of residual units is expressed as follows: before logging data passing through the residual units to reach the private layers of reservoir parameters, the extracted information is recorded as $X_p$, and the operation process of residual units can be expressed as follows:

$$X_{q+1} = \mathrm{h}(X_p) + F(X_q, W_q, b_q) \tag{1}$$

$$X' = f_{ReLU}(X_{q+1}) = max(0, X_{q+1}) \tag{2}$$

$$X' = f_{ReLU}(h(X_p) + F(X_q, W_q, b_q)) \tag{3}$$

Where $X_q$ and $X_{q+1}$ are the input (when q = 1, $X_1$ = X) and output of the q-th hidden layer, respectively; $X_p$ and $X_{q+1}$ are the input and output of the last residual unit, respectively; $W_q$ is the weight of the q-th hidden layer; $b_q$ is the bias of the $q$-th hidden layer; $F$ is an operation function of hidden layers, including the linear operation between hidden layers (i.e. $W_i \cdot X_i^{\mathrm{T}} + b_i = \sum_{j=1}^{m} w_i^j x_i^j + b_i$) and nonlinear operation (i.e., activation function) (Michael, 2015; Goodfellow et al., 2016); the linear operation of the input data of the residual unit in the shortcut layer (i.e. the input and output information of the residual unit are in the same dimension).

### 2.2. Petrophysical constraint

The inclusion of petrophysical information is crucial in the loss function as it significantly impacts the update of model parameters. To improve the accuracy of reservoir parameter prediction, we integrate petrophysical information into the loss function. This has a significant impact on the training of the model and the replacement of its parameters, ultimately leading to the development of a hybrid reservoir parameter prediction neural network that combines data-driven and mechanism-based models. The specific forms of the petrophysical constraints vary depending on the type of petrophysical information and data-driven loss function used. Different forms of petrophysical constraints exist for varying petrophysical information and data-driven loss functions.

#### 2.2.1. Petrophysical constraint in equation form

If we express the petrophysical information in mathematics, it can be broadly categorized into two groups: equality and inequality formulations., Equality formations are generally more precise in describing the petrophysical relationships between the data. In reservoir parameter prediction, the logging response functions are the typical example of equality formations for petrophysical information.

The logging response function can be used to obtain the mechanism model-based reservoir parameter expression. This function depends on logs, reservoir parameters, and regional interpretation parameters, and is denoted as $F_{PI}()$. For example, the commonly used density logging response equation of oil and gas-bearing shaly sand (Eq. (4)) can be transformed into the apparent porosity function (Eq. (5)). This is further denoted as $F_{PI}(x, Y, Z)$ (Eq. (6)), where $x$ is the logs, $Y$ is the reservoir parameters, and $Z$ is the regional interpretation parameters.

$$\rho_b = (1 - V_{sh} - \varphi)\rho_{ma} + V_{sh}\rho_{sh} + \varphi S_{hr}\rho_{hr} + \varphi(1 - S_{hr})\rho_{mf} \tag{4}$$

$$\varphi = \frac{\rho_{ma} - \rho_b + V_{sh}(\rho_{sh} - \rho_{ma})}{\rho_{ma} - \rho_{mf} + S_{hr}(\rho_{mf} - \rho_{hr})} \tag{5}$$

$$F_{PI}(x, Y, Z) = \frac{Z^{\rho_{ma}} - x^{\rho_b} + Y^{V_{sh}}(Z^{\rho_{sh}} - Z^{\rho_{ma}})}{Z^{\rho_{ma}} - Z^{\rho_{mf}} + Y^{S_{hr}}(Z^{\rho_{mf}} - Z^{\rho_{hr}})} \tag{6}$$

Where $\rho_b$ is the density, $V_{sh}$ is shale volumetric concentration, $\varphi$ is porosity, $S_{hr}$ is the residual hydrocarbon saturation of the flushing zone, $\rho_{ma}$ is matrix density, $\rho_{mf}$ is mud filtrate density, $\rho_{sh}$ is shale density, and $\rho_{hr}$ is the residual hydrocarbon density in the flushing zone.

The equation form of the petrophysical information is $F_{PI}$. The data-driven loss function and the petrophysical constraints need to be calculated in the same metric space to ensure consistency. Thus, the petrophysical constraints correspond to the data-driven loss function. Take reservoir parameters prediction as the example, which is a typical regression problem, and the common data-driven loss functions for this problem are root mean squared error (RMSE), mean squared error (MSE), mean absolute error (MAE), and mean absolute percentage error (MAPE). If $F_{PI}$ is the calculated reservoir parameter by the logging response equation, we can construct the corresponding petrophysical

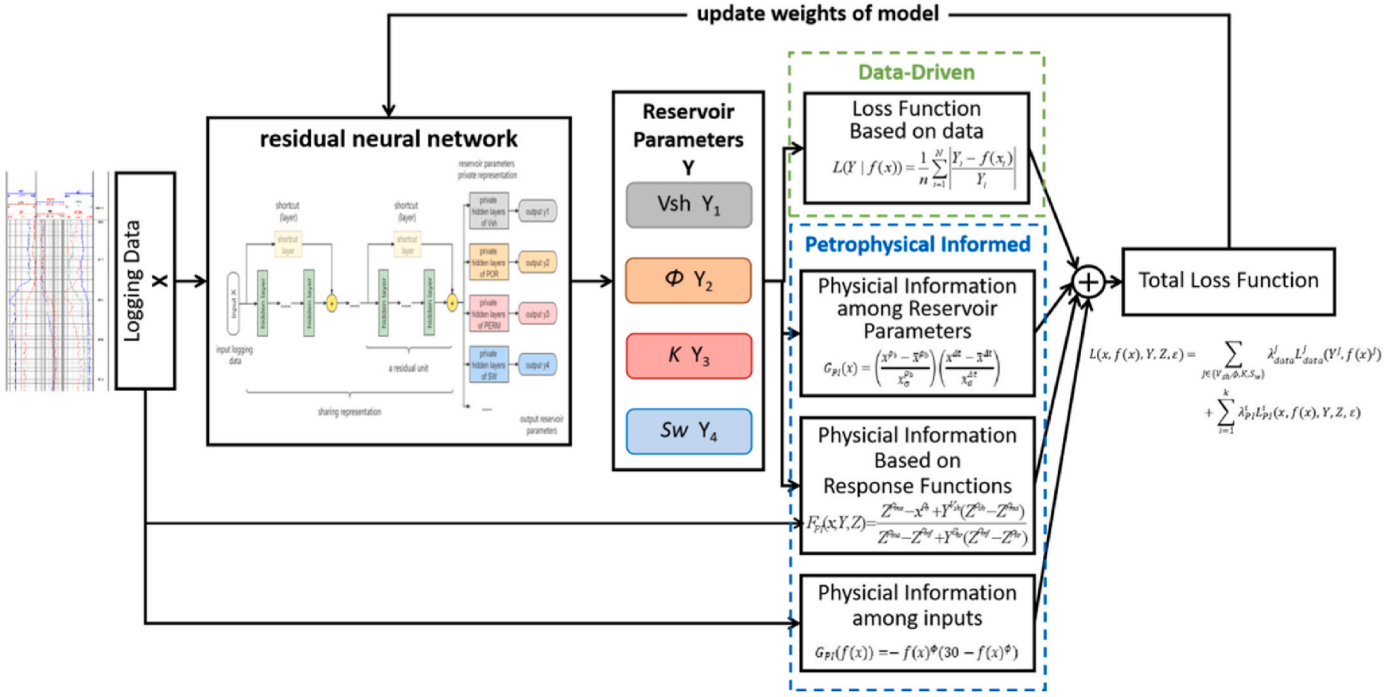


**Fig. 2.** Petrophysical informed residual neural network for multi-task reservoir parameter prediction with the data-mechanism-driven loss function.

constraints based on the calculation method of data-driven loss function. Using the RMSE as a reference, the distance between model output and theoretical reservoir parameters is calculated in the Euclidean domain, and the petrophysical constraints matching the RMSE data-driven loss function are given in Eq. (7). The petrophysical constraint form for MSE is Eq. (8), while the form of petrophysical constraint for MAE is Eq. (9). Referring to MAPE, the petrophysical constraint form is Eq. (10).

$$L_{PI}(x,f(x),Y,Z,\varepsilon)=\sqrt{\frac{1}{n}\sum_{i=1}^{N}f_{ReLU}\left(\left(f(x)_i-F_{PI}(x_i,Y_i,Z_i)\right)^2-\varepsilon\right)} \tag{7}$$

$$L_{PI}(x,f(x),Y,Z,\varepsilon)=\frac{1}{n}\sum_{i=1}^{N}f_{ReLU}\left(\left(f(x)_i-F_{PI}(x_i,Y_i,Z_i)\right)^2-\varepsilon\right) \tag{8}$$

$$L_{PI}(x,f(x),Y,Z,\varepsilon)=\frac{1}{n}\sum_{i=1}^{N}f_{ReLU}\left(\left|f(x)_i-F_{PI}(x_i,Y_i,Z_i)\right|-\varepsilon\right) \tag{9}$$

$$L_{PI}(x,f(x),Y,Z,\varepsilon)=\frac{1}{n}\sum_{i=1}^{N}f_{ReLU}\left(\left|1-\frac{f(x)_i}{F_{PI}(x_i,Y_i,Z_i)}\right|-\varepsilon\right) \tag{10}$$

Where $f(x)$ is the model output, also named as the predicted value; $N$ is the number of samples; $\varepsilon$ pis the allowable error range of petrophysical constraints. Since the regional interpretation parameters $Z$ are fixed, the calculated reservoir parameter using the logging response equation may not be accurate. Therefore, we set an allowable error range for the petrophysical constraints to reduce the deviation of the loss function caused by the inaccurate calculation. If the error between the calculated reservoir parameter and the model outputs falls within the allowable range, $L_{PI}()$ is 0.

### 2.2.2. *Petrophysical constraint in inequation form*

Petrophysical information in inequality is more abstract than the information expressed in equality. It usually represents the relationship between reservoir parameters and logging response values or the range of various data values. We usually transform this information into a function that is always less than zero under normal circumstances, which is denoted as $G_{PI}$. For example, to transfer petrophysical information "porosity range always between 0 and 30 %" to the petrophysicial constraint, we can use Eq. (11). This information is limited to the range of reservoir parameters and is only relevant to the model output. When the porosity prediction $f(x)^{\varphi}$ is between 0 and 30, $G_{PI}(f(x))$ is less than zero. When the $f(x)^{\varphi}$ is greater than 30 or less than 0, $G_{PI}(f(x))$ is greater than 0, and the more out of range, the larger $G_{PI}(f(x))$ is,

$$G_{PI}(f(x))=-f(x)^{\varphi}(30-f(x)^{\varphi}) \tag{11}$$

If the information suggestes that "the trend of density logging and acoustic travel time logging is roughly the same", it can be expressed as Eq. (12). This information only pertains to the logs. Both acoustic travel time log and density log are associated with porosity. Acoustic travel time log exhibits a negatively correlation with porosity, while density log shows a positive correlation with porosity. Therefore, acoustic travel time log and density log are typically negatively correlated with each other. Eq. (12) normalizes each log separately and then multiplies them. The normalized data is scaled into an interval with a mean of 0 and a variance of 1. If the acoustic travel time log and density log meet an overall negative correlation trend, then $G_{PI}(x)$ will be negative. However, if two log curves meet an overall positive correlative trend, $G_{PI}(x)$ will be positive.

$$G_{PI}(x)=\left(\frac{x^{\rho_b}-\overline{x}^{\rho_b}}{x_{\sigma}^{\rho_b}}\right)\left(\frac{x^{\Delta t}-\overline{x}^{\Delta t}}{x_{\sigma}^{\Delta t}}\right) \tag{12}$$

Where $x^{\rho_b}$ is density logs; $\overline{x}^{\rho_b}$ is the mean of density logs; $x_{\sigma}^{\rho_b}$ is the variance of density logs; $x^{\Delta t}$ is acoustic travel time logs; $\overline{x}^{\Delta t}$ is the mean of acoustic travel time logs; $x_{\sigma}^{\Delta t}$ is the variance of acoustic travel time logs.

Similar to the petrophysical constraints in the equation form, the petrophysical constraints in the inequation form also need to be constructed based on the data-driven loss function. Eq. (13) and (14) are the forms of inequality petrophysical constraint corresponding to RMSE and MSE, respectively. Eq. (15) and (16) represent the forms of petrophysical constraint corresponding to MAE and MAPE, respectively.


**Fig. 3.** Data distribution and cross-plot of the oilfield measured logging dataset. (a) The oilfield logging data distribution and cross-plot, including acoustic travel time (AC), caliper (CAL), compensated neutron (CNL), bulk density log (DEN), gamma ray (GR), deep resistivity (RT), and spontaneous potential (SP). (b) Distribution and cross-plot of reservoir parameters.

**Table 1**
Construction method and parameters of neural network model for reservoir parameter prediction using oilfield data. For the transfer learning, the part in bold of the source model and target model is the transferred parameters.

| dataset | Method | Name | Model structure | parameters | optimizer |
|---|---|---|---|---|---|
| Oilfield measured data | Multi-DNN | DNN_a | 7-32-16-32-4*(8–1) | 2420 | Adam |
| | PI-DNN | PI_DNN_a | 7-32-16-32-4*(8–1) | 2420 | |
| | Multi-ResNN | ResNN_a | ↗32↘ 7-32-16-32-4*(8–1) | 2676 | |
| | PI-ResNN | PI_ResNN_a | ↗32↘ 7-32-16-32-4*(8–1) | 2676 | |
| | Transfer-DNN | DNN_source_a | **7–32–16–32**-8-1 | 1601 | Adam |
| | | DNN_target_ft_a | **7–32–16–32**-3*(8–1) | 2147 | Adam + fine-tune |
| | | DNN_target_fz_a | **7–32–16–32**-3*(8–1) | 2147 | Adam + freezing |
| | Transfer-ResNN | ResNN_source_a | **↗32↘** **7–32–16–32**-8-1 | 1857 | Adam |
| | | ResNN_target_ft_a | **↗32↘** **7–32–16–32**-3*(8–1) | 2403 | Adam + fine-tune |
| | | ResNN_target_fz_a | **↗32↘** **7–32–16–32**-3*(8–1) | 2403 | Adam + freezing |

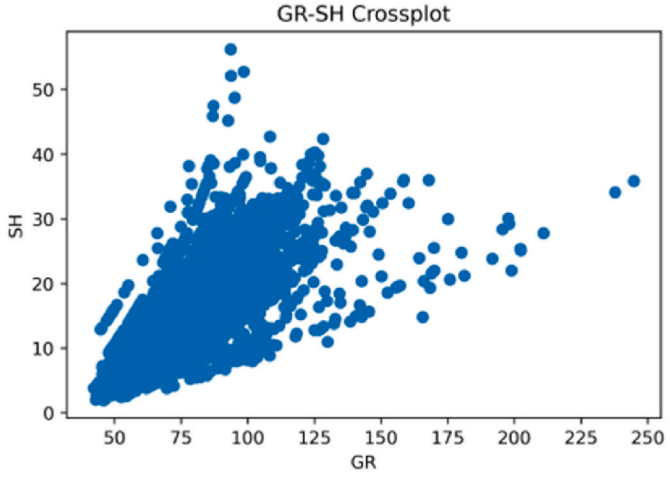


**Fig. 4.** Cross-plot between gamma ray and shale volumetric concentration from the oilfield dataset.

$$L_{PI}(x,f(x),Y,Z,\varepsilon)=\sqrt{\frac{1}{n}\sum_{i=1}^{N}f_{ReLU}(G_{PI}(x_i,Y_i,Z_i)-\varepsilon)^2} \tag{13}$$

$$L_{PI}(x,f(x),Y,Z,\varepsilon)=\frac{1}{n}\sum_{i=1}^{N}f_{ReLU}(G_{PI}(x_i,Y_i,Z_i)-\varepsilon)^2 \tag{14}$$

$$L_{PI}(x,f(x),Y,Z,\varepsilon)=\frac{1}{n}\sum_{i=1}^{N}f_{ReLU}(G_{PI}(x_i,Y_i,Z_i)-\varepsilon) \tag{15}$$

$$L_{PI}(x,f(x),Y,Z,\varepsilon)=\frac{1}{n}\sum_{i=1}^{N}f_{ReLU}\left(\frac{|f(x)_i|}{G_{PI}(x_i,Y_i,Z_i)}-\varepsilon\right) \tag{16}$$

### 2.3. The data-mechanism-driven loss function

Fig. 2 shows the structure of petrophysical informed residual neural network for multi-task reservoir parameter prediction. This model achieves data-mechanism-driven behavior through the fusion of data-driven loss function and petrophysical constraint. For the logging reservoir parameter prediction, considering, petrophysical constraints can be categorized into three types based on the data types involved in the petrophysical information:

**Table 2**
Evaluation Metrics of various models on the test set of field data. The total MAE is the sum of MAE values for the four reservoir parameters. The total MAPE and total $R^2$ score are the mean values of the four reservoir parameter evaluation indicators. The MSE ± std is not averaged or summed, but instead shows the mean square error (MSE) with its corresponding standard deviation (std).

| Model | | MAE | MSE ± std | MAPE | R2 |
|---|---|---|---|---|---|
| DNN_a | SH | 2.679 | 15.39 ± 3.82 | 17.37 | 0.663 |
| | POR | 0.505 | 0.527 ± 0.685 | 5.524 | 0.927 |
| | PERM | 0.063 | 0.0337 ± 0.18 | 20.31 | 0.542 |
| | SW | 6.077 | 72.33 ± 8.425 | 9.122 | 0.743 |
| | **Total** | 9.324 | – | 13.08 | 0.719 |
| PI_DNN_a | SH | 2.276 | 12.178 ± 3.45 | 14.85 | 0.733 |
| | POR | 0.437 | 0.4368 ± 0.60 | 4.916 | 0.950 |
| | PERM | 0.051 | 0.0337 ± 0.19 | 16.49 | 0.509 |
| | SW | 5.551 | 63.952 ± 7.87 | 8.263 | 0.775 |
| | **Total** | 8.315 | – | 11.13 | 0.742 |
| ResNN_a | SH | 2.599 | 14.60 ± 3.8 | 16.78 | 0.680 |
| | POR | 0.552 | 0.5741 ± 0.74 | 6.141 | 0.921 |
| | PERM | 0.059 | 0.024 ± 0.15 | 25.77 | 0.671 |
| | SW | 5.974 | 70.44 ± 8.22 | 8.888 | 0.752 |
| | **Total** | 9.184 | – | 14.3 | 0.756 |
| PI_ResNN_a | SH | 2.257 | 12.60 ± 3.54 | 14.93 | 0.724 |
| | POR | 0.453 | 0.42 ± 0.684 | 4.988 | 0.942 |
| | PERM | 0.055 | 0.03 ± 0.171 | 16.31 | 0.572 |
| | SW | 5.073 | 50.48 ± 7.09 | 7.596 | 0.822 |
| | **Total** | 7.837 | – | 10.96 | 0.765 |
| DNN_source_a | SH | 2.311 | 14.29 ± 3.70 | 14.58 | 0.687 |
| DNN_target_ft_a | POR | 0.459 | 0.431 ± 0.654 | 5.267 | 0.941 |
| | PERM | 0.050 | 0.028 ± 0.163 | 16.95 | 0.624 |
| | SW | 4.973 | 52.99 ± 7.19 | 7.320 | 0.813 |
| | **Total** | 5.482 | – | 9.846 | 0.793 |
| DNN_target_ fz_a | POR | 0.458 | 0.431 ± 0.656 | 5.276 | 0.941 |
| | PERM | 0.049 | 0.022 ± 0.147 | 16.59 | 0.698 |
| | SW | 5.505 | 72.549 ± 8.4 | 8.736 | 0.745 |
| | **Total** | 6.012 | – | 10.20 | 0.794 |
| ResNN_source_a | SH | 2.253 | 13.486 ± 3.63 | 14.74 | 0.704 |
| ResNN_target_ft_a | POR | 0.463 | 0.448 ± 0.669 | 5.348 | 0.938 |
| | PERM | 0.047 | 0.0184 ± 0.1 | 17.46 | 0.750 |
| | SW | 5.629 | 72.236 ± 8.30 | 9.098 | 0.746 |
| | **Total** | 6.139 | – | 10.64 | 0.811 |
| ResNN_target_fz_a | POR | 0.461 | 0.445 ± 0.667 | 5.246 | 0.939 |
| | PERM | 0.051 | 0.023 ± 0.15 | 19.01 | 0.684 |
| | SW | 5.725 | 68.74 ± 8.24 | 8.889 | 0.758 |
| | **Total** | 6.237 | – | 11.05 | 0.794 |

(1). Constraints related only to the input data that check the logs' compliance, and often in the form of inequality petrophysical constraint;
(2). Constraints related only to the output data that restrict the reservoir parameters to a reasonable range, also in the form of the inequality petrophysical constraint;

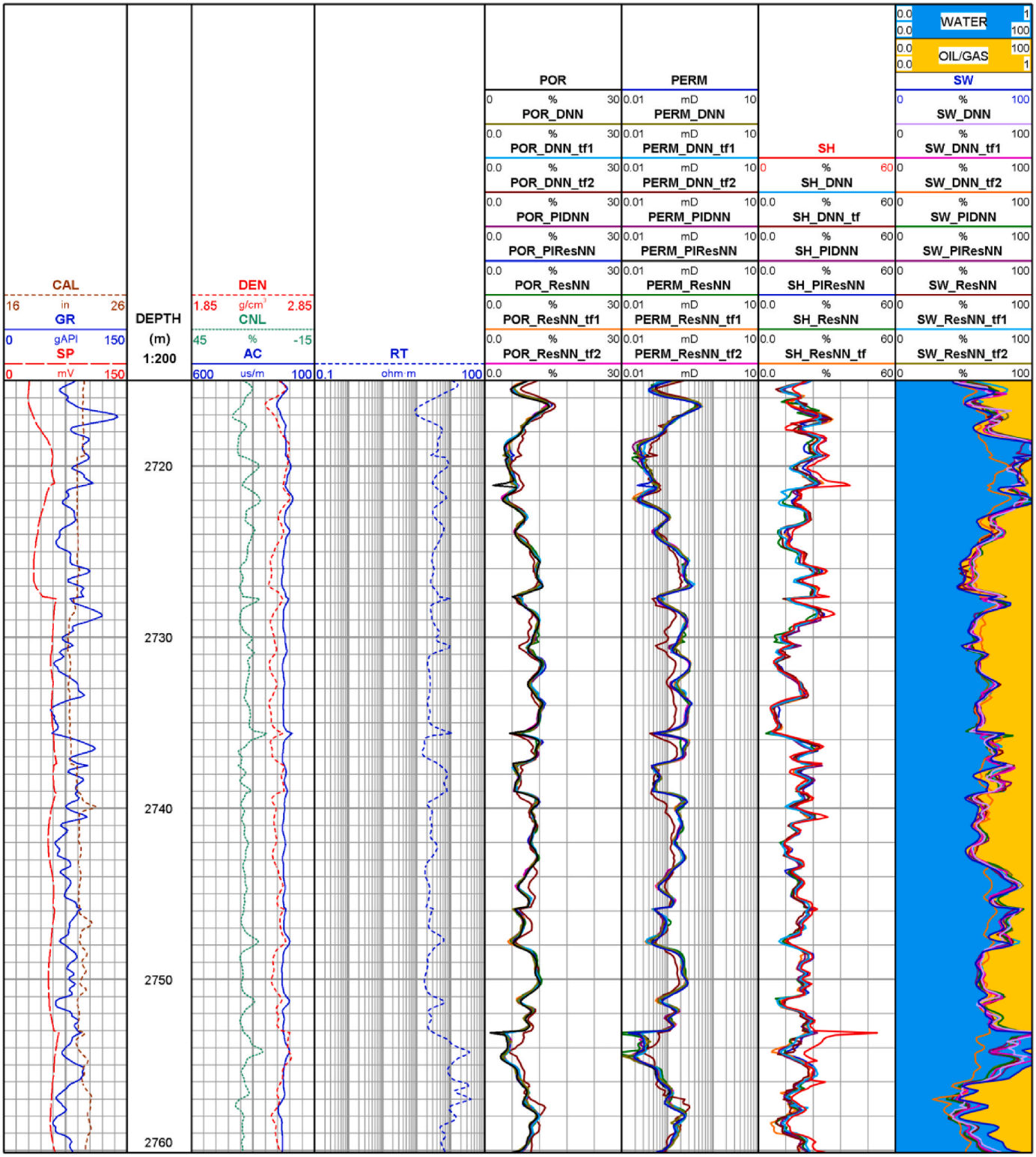


**Fig. 5.** The application effect of different reservoir parameter prediction neural networks constructed or trained by various methods. The lithologic logs (SP, GR, CAL), resistivity log (RT), and porosity logs (CNL, DEN, AC) are used as features, while SH, POR, PERM, and SW are the labeled reservoir parameters. The suffixes of reservoir parameters represent the different models. For the transfer learning model, the suffixes are 'tf', where 'tf' is the source model used for SH prediction. 'tf1' and 'tf2'are fine-tuning training and freezing training models used for other reservoir parameters prediction, respectively. The figure illustrates the actual application effect of the different models trained by oilfield data on one well in the test set.

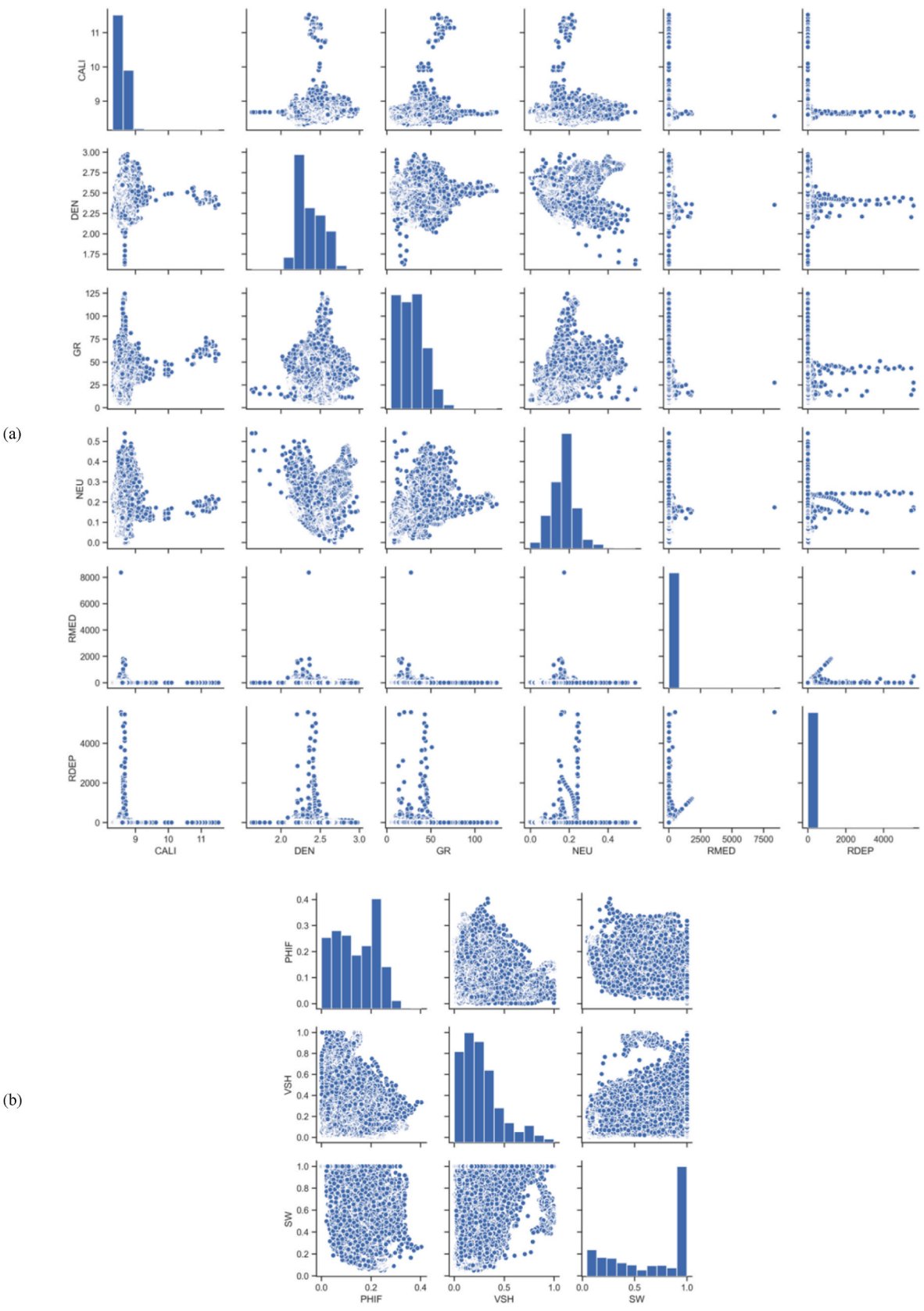


**Fig. 6.** Data distribution and cross-plot of the 2021 SPWLA PAAD competition dataset from the Society of Petrophysics and Well Log Analysts (SPWLA). (a)Distribution and cross-plot of logs, including caliper (CALI), bulk density log (DEN), gamma ray (GR), neutron porosity (NEU), medium resistivity (RMED), and deep resistivity (RDEP). (b) Distribution and cross-plot of reservoir parameters including porosity (PHIF), shale volumetric concentration (VSH), and water saturation (SW).

**Table 3**
Construction method and parameters of neural network model for reservoir parameter prediction using SPWLA PDDA machine learning competition data. For the transfer learning, the part in bold of the source model and target model is the transferred parameters.

| dataset | Method | Name | Model structure | parameters | optimizer |
|---|---|---|---|---|---|
| SPWLA PDDA | Multi-DNN | DNN_b | 6-32-16-32-3*(8-4-1) | 2211 | Adam |
| | PI-DNN | PI_DNN_b | 6-32-16-32-3*(8-4-1) | 2211 | |
| | Multi-ResNN | ResNN_b | ↗32↘ 6-32-16-32-3*(8-4-1) | 2435 | |
| | PI-ResNN | PI_ResNN_b | ↗32↘ 6-32-16-32-3*(8-4-1) | 2435 | |
| | Transfer-DNN | DNN_source_b | **6–32–16–32**-8-4-1 | 1601 | Adam |
| | | DNN_target_ft_b | **6–32–16–32**-2*(8-4-1) | 1906 | Adam + fine-tune |
| | | DNN_target_fz_b | **6–32–16–32**-2*(8-4-1) | 1906 | Adam + freezing |
| | Transfer-ResNN | ResNN_source_b | ↗**32**↘ **6–32–16–32**-8-4-1 | 1825 | Adam |
| | | ResNN_target_ft_b | ↗**32**↘ **6–32–16–32**-2*(8-4-1) | 2130 | Adam + fine-tune |
| | | ResNN_target_fz_b | ↗**32**↘ **6–32–16–32**-2*(8-4-1) | 2130 | Adam + freezing |

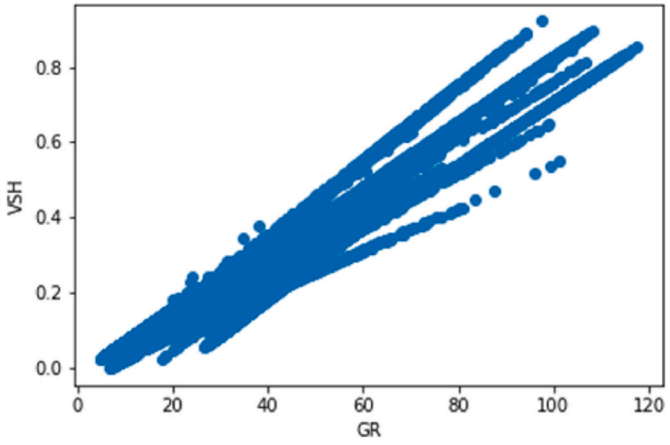


**Fig. 7.** Cross-plot for gamma ray and shale volumetric concentration in the 2021 SPWLA PDDA competition dataset.

(3). Constraints related to both input and output data that enforce the relationship between logs and reservoir parameters to fit existing cognition, expressed as both equation and inequation forms. These three types of rock physical constraints are uniformly represented as $L_{PI}()$. Eq. (17) shows the total loss function with data-driven loss function and petrophysical constraints,

$$L(x,f(x),Y,Z,\varepsilon) = \sum_{j\in\{V_{sh},\varphi,K,S_w\}} \lambda^j_{data} L^j_{data}\left(Y^j, f(x)^j\right) + \sum_{i=1}^{k} \lambda^i_{PI} L^i_{PI}(x,f(x),Y,Z,\varepsilon) \tag{17}$$

Where $x$ is input logging data, $Y$ is the labeled reservoir parameters, $f(x)$ is the model output, $Z$ is the physical parameters used in the petrophysical constraint, and $\varepsilon$ is the allowable error ranges of the petrophysical constraint. $V_{sh}$, $K$, and $S_w$ are shale volumetric concentration, porosity, permeability, and water saturation, respectively. $\lambda^j_{data}$ is the weight of the data-driven loss function, and $L^j_{data}$ is the data-driven loss function of different reservoir parameters. The total number of petrophysical constraints is k and $\lambda^i_{PI}$ is the i-th weight of petrophysical constraint. $L^i_{PI}()$ is the i-th petrophysical constraint.

## 3. Case study

In this section, we aim to demonstrate how incorporating logging domain knowledge can improve the performance of the reservoir evaluation model. We use different types of logging data from two separate areas. The first dataset is obtained from an oil field in China and we want to predict porosity, permeability, shale volumetric concentration, and water saturation. The second dataset is provided by the Petrophysical Data Driven Analytics (PDDA) machine learning competition 2021, organized by the Society of Petrophysicists and Well Log Analysts (SPWLA). We aim to predict porosity, water saturation, and shale volumetric concentration (SPWLA, 2021). We compare the performance of the multi-task neural network and multi-task residual neural network with and without petrophysical petrophysical constraints on the two logging datasets. In addition, we analyze the impact of different combinations of petrophysical mechanism models on the overall performance of the model.

**Table 4**
Evaluation Metrics for various models on the test set in the 2021 SPWLA PADD competition data.

| Model | | MAE | MSE ± std | MAPE | R2 |
|---|---|---|---|---|---|
| DNN_b | PHIF | 0.006 | 9.8e-5±0.01 | 9.208 | 0.980 |
| | VSH | 0.053 | 0.0041 ± 0.07 | 24.79 | 0.918 |
| | SW | 0.015 | 0.0014 ± 0.04 | 3.373 | 0.987 |
| | **Total** | 0.074 | – | 12.457 | 0.962 |
| PI_DNN_b | PHIF | 0.005 | 6.5e-5±0.01 | 8.321 | 0.987 |
| | VSH | 0.048 | 0.0048 ± 0.07 | 19.472 | 0.912 |
| | SW | 0.011 | 0.0008 ± 0.03 | 2.467 | 0.992 |
| | **Total** | 0.063 | – | 10.087 | 0.964 |
| ResNN_b | PHIF | 0.009 | 1.9e-4±0.01 | 11.380 | 0.960 |
| | VSH | 0.05 | 0.0046 ± 0.07 | 22.364 | 0.914 |
| | SW | 0.018 | 0.0020 ± 0.04 | 4.479 | 0.982 |
| | **Total** | 0.081 | – | 12.741 | 0.952 |
| PI_ResNN_b | PHIF | 0.004 | 6.2e-5±0.01 | 6.706 | 0.978 |
| | VSH | 0.046 | 0.0046 ± 0.07 | 18.935 | 0.914 |
| | SW | 0.012 | 0.0008 ± 0.03 | 2.915 | 0.992 |
| | **Total** | 0.062 | – | 9.519 | 0.961 |
| DNN_source_b | SH | 0.049 | 0.0045 ± 0.07 | 18.761 | 0.917 |
| DNN_target_ft_b | PHIF | 0.005 | 8.0e-5±0.01 | 8.300 | 0.983 |
| | SW | 0.012 | 0.0009 ± 0.03 | 2.680 | 0.991 |
| | **Total** | 0.016 | – | 5.49 | 0.987 |
| DNN_target_fz_b | PHIF | 0.005 | 7.6e-5±0.01 | 8.792 | 0.984 |
| | SW | 0.012 | 0.0009 ± 0.03 | 2.716 | 0.992 |
| | **Total** | 0.017 | – | 5.754 | 0.988 |
| ResNN_source_b | SH | 0.048 | 0.0039 ± 0.06 | 20.371 | 0.928 |
| ResNN_target_ft_b | PHIF | 0.005 | 5.9e-5±0.01 | 7.533 | 0.988 |
| | SW | 0.013 | 0.0009 ± 0.03 | 2.956 | 0.992 |
| | **Total** | 0.018 | – | 5.245 | 0.990 |
| ResNN_target_fz_b | PHIF | 0.005 | 7.6e-5±0.01 | 8.846 | 0.984 |
| | SW | 0.013 | 0.0010 ± 0.03 | 2.986 | 0.990 |
| | **Total** | 0.019 | – | 5.916 | 0.987 |

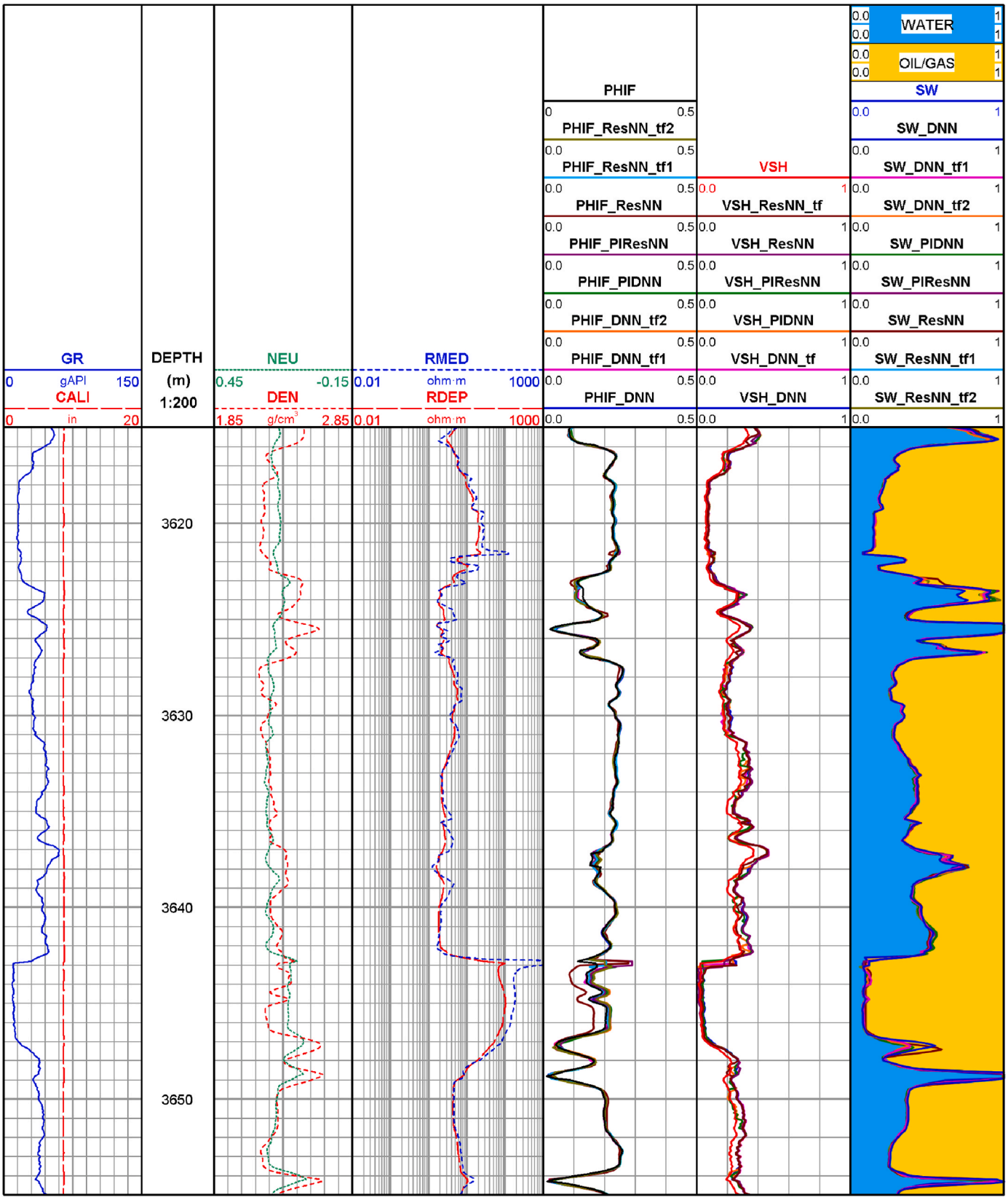


**Fig. 8.** The application effect of various reservoir parameter prediction neural networks constructed or trained using different methods. The lithologic logs (GR, CALI) resistivity logs (RMED, RDEP), and porosity logs (DEN, NEU) are used as features, while PHIF, VSH, and SW are the labeled reservoir parameters. The suffixes of reservoir parameters represent the different models. For the transfer learning model, the suffixs are 'tf', where 'tf' is the source model used for VSH prediction, 'tf1' and 'tf2' are fine-tuning training and freezing training models used for other reservoir parameters prediction, respectively. The figure illustrates the actual application effect of the different models trained by SPWLA PDDA machine learning competition data on one well in the test set.

**Table 5**
Performance of reservoir parameters prediction of the residual neural network model with petrophysical constraints with different $\lambda_{PI}$.

| $\lambda_{PI}$ | Out-put | MAPE_AVG | MAPE | MAE | MSE ± std | $R^2$ |
|---|---|---|---|---|---|---|
| 0 | SH | 13.72 | 16.70 | 2.59 | 15.35 ± 3.83 | 0.663 |
| | POR | | 10.74 | 0.913 | 1.429 ± 1.195 | 0.803 |
| 0.01 | SH | 11.70 | 15.28 | 2.51 | 15.09 ± 3.84 | 0.683 |
| | POR | | 8.12 | 0.621 | 0.986 ± 0.993 | 0.864 |
| 0.02 | SH | 11.49 | 15.35 | 2.42 | 14.40 ± 3.68 | 0.684 |
| | POR | | 7.64 | 0.678 | 1.012 ± 1.005 | 0.860 |
| 0.05 | SH | 10.61 | 15.36 | 2.33 | 13.48 ± 3.65 | 0.704 |
| | POR | | 5.86 | 0.529 | 0.577 ± 0.756 | 0.920 |
| 0.1 | SH | 11.03 | 15.29 | 2.40 | 14.17 ± 3.64 | 0.689 |
| | POR | | 6.76 | 0.609 | 0.777 ± 0.879 | 0.893 |
| 0.2 | SH | 12.20 | 16.09 | 2.52 | 15.14 ± 3.81 | 0.668 |
| | POR | | 8.31 | 0.715 | 0.914 ± 0.953 | 0.874 |
| 0.5 | SH | 13.21 | 16.48 | 2.63 | 15.85 ± 3.83 | 0.652 |
| | POR | | 9.946 | 0.865 | 1.320 ± 1.146 | 0.818 |

### 3.1. Oilfield measured data

#### 3.1.1. Data description

The first dataset consists of conventional logs obtained from a tight sandstone shale oil and gas reservoir with low porosity, low permeability, and low contrast. Logs include acoustic travel time (AC), compensated neutron (CNL), bulk density log (DEN), caliper (CAL), gamma ray (GR), spontaneous potential (SP), and deep resistivity (RT). The reservoir parameters we want to predicate are shale volumetric concentration (SH), porosity (POR), permeability (PERM), and water saturation (SW). The distribution ranges of SH, POR, PERM, and SW are 16.61 ± 6.60 (%),9.71 ± 2.70 (%), 0.233 ± 0.255 (mD), and 66.60 ± 16.74 (%). Since the experiment involves the fusion of petrophysics knowledge and data-driven model through loss function, data normalization, standardization and other scaling processing are not suitable. After removing the missing value and outliers, more than 5000 labels are used for the model training and testing. Fig. 3a shows the distribution and cross-plot of logs, Fig. 3b shows the distribution and cross-plot of reservoir parameters.

#### 3.1.2. Model construction and training

In this case study, two basic models are used: multi-task deep neural network (Multi_DNN) and multi-task residual neural network (Multi_ResNN). One of the key advantages of the multi-task model in the context of data-mechanism driven reservoir parameter prediction is that different predication tasks are interconnected. Petrophysical constraints can impact one reservoir parameter task, but they can also affect the predictions of other reservoir parameters. In the task of predicting reservoir parameters, logging response functions demonstrate that the parameters such as porosity and shale volumetric concentration have the approximately linear relationship with multiple logging curves. Therefore, the residual structure in the neural network is expected to improve the model's ability to fit this linear relationship.

Transfer learning also can incorporate petrophysical information into the neural network by leveraging the known relationship between reservoir parameters to improve the performance of the model in the target domain. In logs' interpretation, the shale volumetric concentration is calculated from gamma ray or spontaneous potential, and the porosity is calculated using the shale-corrected porosity logs (acoustic travel time, compensated neutron and density). Finally, the porosity, shale volumetric concentration, and resistivity logs are used to calculate the water saturation and other relevant information. We set the shale volumetric concentration prediction model as the source model, and other reservoir parameters prediction model as the target model, using the knowledge gained from the source model to improve the performance of the target model. There are two methods for training the transferred parameters in transfer learning: parameter freezing and fine-tuning. In parameter freezing, the transferred parameters are fixed, and only other parameters are iterated during the target model training. In the parameter fine-tuning, some or all the transferred parameters participate in the parameter iteration of the target model training.

We use Adam optimizer (Kingma and Ba, 2014) in the training process. By setting the hyper-parameter and using the Adam algorithm, the updating step size can be automatically calculated. The step size decreases when the noise is high and the step size increases when the noise is low, allowing the model to approach the optimal point quickly and stably.

Table 1 lists a statistical summary of the model used in this section.

Reservoir parameters are typically handled in multi-task reservoir parameter prediction using a normalization method that unifies the data scale such that there is no order of magnitude difference in the loss function between tasks. In addition, adjusting the $\lambda_{data}$ also could balance the differences between the loss functions between different reservoir parameters. In the experiments, since the logging response functions we added will use model outputs, it is not appropriate to normalise the reservoir parameters.The MAPE loss function calculates the percentage difference between the outputs and the tagged values, which means that the loss function does not vary by several orders of magnitude on the reservoir parameter even though it is not normalized for the reservoir parameter. And the weights of the data-driven loss function can all be set to 1. In the petrophysical informed model, we use the gamma ray logging response function to calculate the shale volumetric concentration. The total loss function is given by Eq. (18),

$$L(x,f(x),Y,Z,\varepsilon)=\frac{1}{n}\sum_{i=1}^{N}\left[\sum_{j\in\{V_{sh},\varphi,K,S_w\}}\left(\frac{\left|f(x)_i^j-Y_i^j\right|}{Y_i^j}\right)+\lambda_{\mathrm{PI}}f_{ReLU}\left(\left|1-\frac{F_{PI}^{V_{sh}}(x_i,Y_i,Z_i)}{f(x)_i^{V_{sh}}}\right|-\varepsilon\right)\right] \tag{18}$$

Where $f(x)_i^{V_{sh}}$ and $F_{PI}^{V_{sh}}(x_i,Y_i,Z_i)$ are the model output shale volumetric concentration and theoretical shale volumetric concentration of i-th sample, respectively; $Y_i^j$ and $f(x)_i^j$ are the label and model output reservoir parameters of i-th sample, respectively. $\lambda_{\mathrm{PI}}$ is the weight of the regularization term and $f_{ReLU}$ is the activation function.

Gamma ray reflects the absorption of formation for gamma, which depends mainly on the formation density. The gamma ray logging response function can be expressed as Eq. (19),

$$GR\rho_b=GR_{ma}\rho_{ma}+V_{sh}(GR_{sh}\rho_{sh}-GR_{ma}\rho_{ma}) \tag{19}$$

Where GR is the gamma ray log, $\rho_b$ is density log, $V_{sh}$ is the shale volumetric concentration, $GR_{ma}$ and $GR_{sh}$ are the gamma ray of matrix and shale respectively, and $\rho_{ma}$ and $\rho_{sh}$ are density log of matrix and shale, respectively.

Using Eq. (19), we can calculate $F_{PI}^{V_{sh}}(x_i,Y_i,Z_i)$ by Eq. (20),

$$F_{PI}^{V_{sh}}(x,Y,Z)=\frac{x^{GR}\,x^{\rho_b}-Z^{GR_{ma}}Z^{\rho_{ma}}}{Z^{GR_{sh}}Z^{\rho_{sh}}-Z^{GR_{ma}}Z^{\rho_{ma}}}\times 100\% \tag{20}$$

Where $GR_{ma}=5.0$, $\rho_{ma}=2.65$, $GR_{sh}=115.0$, $\rho_{sh}=2.96$.

#### 3.1.3. Model construction and training

In the experiment, the training set and test set are split in a ratio of 4:1. The used optimizer is Adam with default hyperparameters. All data-driven models use MAPE as loss functions. The number of epochs is 10000 and the batch size is 100. The two models with the petrophysical constraint, PI_DNN_a and PI_ResNN_a, use the same total loss function which is represented in Eq. (22). The two parameters $\lambda_{\mathrm{PI}}$ and $\varepsilon$ control the addition of petrophysical information. A higher $\lambda_{\mathrm{PI}}$ results in a greater influence of the petrophysical information, while a higher $\varepsilon$ allows for a greater allowable error range of the mechanism model. Based on the cross-plot of gamma ray - shale volumetric concentration in Fig. 4, gamma ray and shale volumetric concentration are positively correlated but with an inconspicuous linear relationship. And $\lambda_{\mathrm{PI}}$ and $\varepsilon$

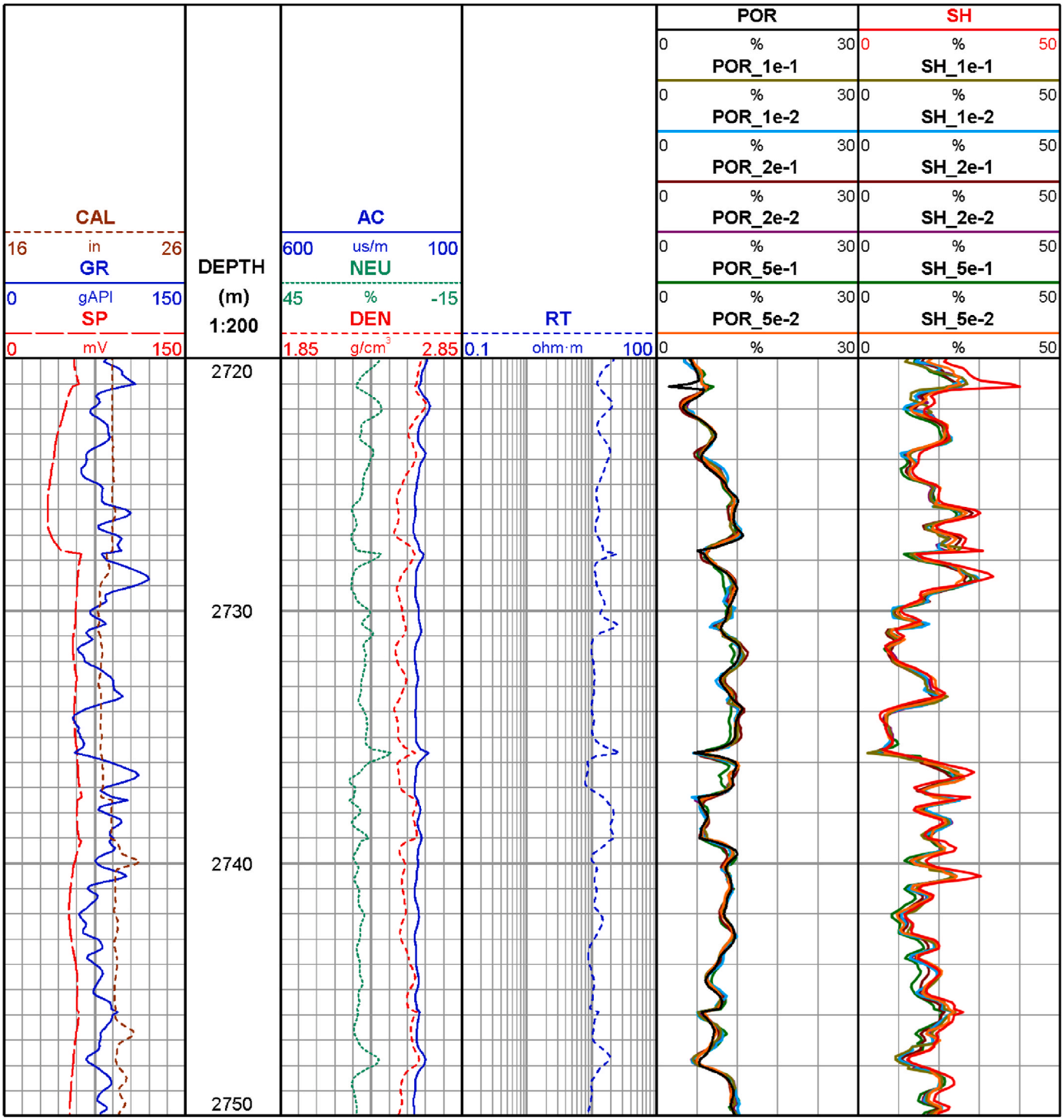


**Fig. 9.** Comparison of application performance of petrophysical informed model with different $\lambda_{PI}$. POR/SH_1e-2, POR/SH_2e-2, POR/SH_5e-2, POR/SH_1e-1, POR/SH_2e-1, and POR/SH_5e-1 represent taking $\lambda_{PI}$ as 0.01, 0.02, 0.05, 0.1, 0.2,0.5 respectively.

are set as 0.1.

To evaluate the effectiveness of a model, it is common to use multiple evaluation indexes since a single index may have some shortcomings. In this experiment, we use several evaluation indexes, including MAE, MSE $\pm$ std, MAPE, and $R^2$ score (Eq. (21)), to comprehensively evaluate the performance of each prediction model for reservoir parameters on the test set. The indexes can not only be used as loss functions, but also for model evaluation. In general, smaller values of MAE, MSE, and MAPE indicate better model performance. The $R^2$ score, which ranges from 0 to 1, reflects the relative contribution of the regression, i.e., the percentage of the total variation in the dependent variable $f(x)$ that can be explained by the regression. The larger the $R^2$ score, the better the model performance.

$$R^2 = \frac{\sum_i (f(x_i) - \overline{Y})^2}{\sum_i (Y_i - \overline{Y})^2} \tag{21}$$

Table 2shows the performance of various models on the test set. The petrophysical informed model generally outperforms pure data-

**Table 6**
Performance of reservoir parameters prediction of the residual neural network model with petrophysical constraints with different $\varepsilon$.

| $\varepsilon$ | Out-put | MAPE_AVG | MAPE | MAE | MSE ± std | $R^2$ |
|---|---|---|---|---|---|---|
| 0.01 | SH | 12.33 | 15.77 | 2.41 | 13.96 ± 3.68 | 0.693 |
| | POR | | 8.890 | 0.773 | 1.144 ± 1.068 | 0.842 |
| 0.02 | SH | 11.19 | 15.44 | 2.43 | 14.60 ± 3.72 | 0.680 |
| | POR | | 6.93 | 0.626 | 0.854 ± 0.914 | 0.883 |
| 0.05 | SH | 10.99 | 15.23 | 2.38 | 14.04 ± 3.64 | 0.692 |
| | POR | | 6.75 | 0.599 | 0.696 ± 0.834 | 0.904 |
| 0.1 | SH | 11.00 | 15.29 | 2.40 | 14.17 ± 3.64 | 0.689 |
| | POR | | 6.72 | 0.607 | 0.867 ± 0.927 | 0.880 |
| 0.2 | SH | 11.38 | 15.88 | 2.47 | 14.31 ± 3.71 | 0.686 |
| | POR | | 6.88 | 0.619 | 0.801 ± 0.895 | 0.889 |
| 0.5 | SH | 11.68 | 15.99 | 2.54 | 14.88 ± 3.75 | 0.673 |
| | POR | | 7.37 | 0.660 | 0.861 ± 0.922 | 0.881 |

driven model, whether based on the deep neural network (DNN) or residual neural network (ResNN) when we predict the four reservoir parameters together. Overall, the MAPE_AVG of the PI_DNN_a model is about 2 % which is lower than that of the DNN_a model, and the MAPE_AVG of the PI_ResNN_a model is about 4 % which is lower than that of the ResNN_a model. Specifically, for DNN based model, the permeability (PERM) prediction performance is most improved, with a decrease in MAPE of about 4 %, while the MAPE of shale volumetric concentration (SH), the main focus of the mechanism model, is decreased by about 2.5 %. For ResNN based model, the PERM prediction performance is also most improved, with a decrease in MAPE of nearly 10 %, and the MAPE of SH is decreased by about 2 %. These experiments suggest that the petrophysical constraint has a more pronounced effect on the ResNN than the DNN. The petrophysical informed model can improve the prediction performance of multiple reservoir parameters in a multi-task model.

Transfer learning divides the reservoir parameters prediction into two models. First, the shale volumetric concentration prediction model is trained, and then the other three reservoir parameters prediction model based is trained based on the transferred parameters from the shale volumetric concentration prediction model. Compared with the multi-task model, the prediction performance of the three reservoir parameters is improved after transfer learning.

The DNN improves more obviously than the ReNN in terms of the improvement effect of reservoir parameters prediction. There is little difference between the performance of the model trained by the fine-tune method and the freezing method, and the fine-tune method is slightly better. Compared with the training method, the model structure and the selection of source and target domains have more influence on the model performance. The prediction performance of the single-task shale volumetric concentration prediction model is obviously better than that of the multi-task model because the assistance of the shale volumetric concentration prediction task from other reservoir parameter prediction tasks in the multi-task model is less than the interference of other tasks with the shale volumetric concentration prediction task. With the help of petrophysical knowledge in the petrophysical constraint, the prediction performance of shale volumetric concentration is similar to that of the single-task model, indicating that the petrophysical constraint can reduce mutual interference in the multi-task model and improve performance.

Although there is little difference between the performances of transfer learning and the petrophysical informed model from the evaluation indicators, transfer learning needs to train two models and decide on the source and target domains. The reservoir parameters prediction process of transfer learning is more complex, and it consumes more computing resources compared with the petrophysical informed model. For the application mechanism of petrophysics knowledge, the petrophysical informed model can select the appropriate mechanism model and control the mechanism model fusion through $\lambda_{PI}$ and $\varepsilon$. On the other hand, the application of transfer learning to petrophysics knowledge is relatively simple, and it cannot accurately fuse petrophysics knowledge with the model. Fig. 5 shows the application of all models trained by field data on one well in the test set.

### 3.2. SPWLA PDDA machine learning competition data

#### 3.2.1. Data description

The second dataset used in the case study is obtained from the Petrophysical Data Driven Analytics (PDDA) machine learning competition 2021, organized by the Society of Petrophysics and Well Log Analysts (SPWLA). The dataset consists of 12 logs, and we select caliper (CALI), bulk density log (DEN), gamma ray (GR), neutron porosity (NEU), deep resistivity (RDEP), and medium resistivity (RMED) for reservoir parameters prediction. After data pre-processing, over 40,000 labels are used in the model for training and testing. Fig. 6a shows the distribution and cross-plot of logs. Reservoir parameters are all less than 1 where PHIF is distributed in the interval of (0, 0.404), VSH in the interval of (0, 1), and SW in the interval of (0.04, 1). Fig. 6b shows the distribution and cross-plot of reservoir parameters. Overall, the first dataset is more evenly distributed, while the second dataset is more widely distributed.

#### 3.2.2. Model construction and training

The SPWLA PDDA dataset is also used for experiments using a model without petrophysical constraints and a transfer learning model. Table 3 lists the models used in this experiment and their settings.

The distribution range of the three reservoir parameters in the 2021 SPWLA PDDA competition dataset is similar and located in the interval (0,1). We use MAE as the data-driven loss function and select the corresponding petrophysical constraint. Eq. (22) gives the total loss function.

$$L(x,f(x),Y,Z,\varepsilon) = \frac{1}{n}\sum_{i=1}^{N}\left[\sum_{j\in\{V_{sh},\varphi,S_w\}}\left|f(x)_i^j - Y_i^j\right| + \lambda_{PI} f_{ReLU}\left(\left|f(x)_i^{V_{sh}} - F_{PI}^{V_{sh}}(x_i,Y_i,Z_i)\right| - \varepsilon\right)\right] \tag{22}$$

Where $f(x)_i^{V_{sh}}$ and $F_{PI}^{V_{sh}}(x_i,Y_i,Z_i)$ are the model output shale volumetric concentration and theoretical shale volumetric concentration of i-th sample, respectively; $Y_i^j$ and $f(x)_i^j$ are the label and model output reservoir parameters of i-th sample, respectively. $\lambda_{PI}$ is the weight of the regularization term and $f_{ReLU}$ is the activation function.

Since there is limited geological or core information, it is difficult to analyze the source of radioactive material in the reservoir. We select a gamma ray logging response function in a more general form,

$$I_{sh} = (GR - GR_{min}) / (GR_{max} - GR_{min}) \tag{23}$$

$$F_{PI}^{V_{sh}} = V_{sh} = \frac{2^{gcur I_{sh}} - 1}{2^{gcur} - 1} \tag{24}$$

Where $I_{sh}$ is the relative value between shale volumetric concentration and gamma ray log. $GR_{min}$ and $GR_{max}$ are gamma ray log of pure sandstone and pure shale. We set $GR_{min} = 1$, $GR_{max} = 130$. *gcur* is the empirical coefficient, which is related to the stratigraphic age. For Tertiary strata, *gcur* = 3.7.

#### 3.2.3. Experimental result

Nine wells in the 2021 SPWLA PDDA competition dataset have labels. We select one well as the test set and the remaining eight wells as the training set. The used optimizer is Adam with the default hyperparameters, and the data-driven loss function of all models are MAE. The number of epochs is 1000 and the batch size is 1000. Two petrophysical informed models, PI_DNN_b and PI_ResNN_b, use the same petrophysical constraint by Eq. (22). Fig. 7 shows the cross-plot of gamma ray and shale volumetric concentration. The correlation between gamma ray and shale volumetric concentration in this data is better than that in the field data in the previous section. Combined with

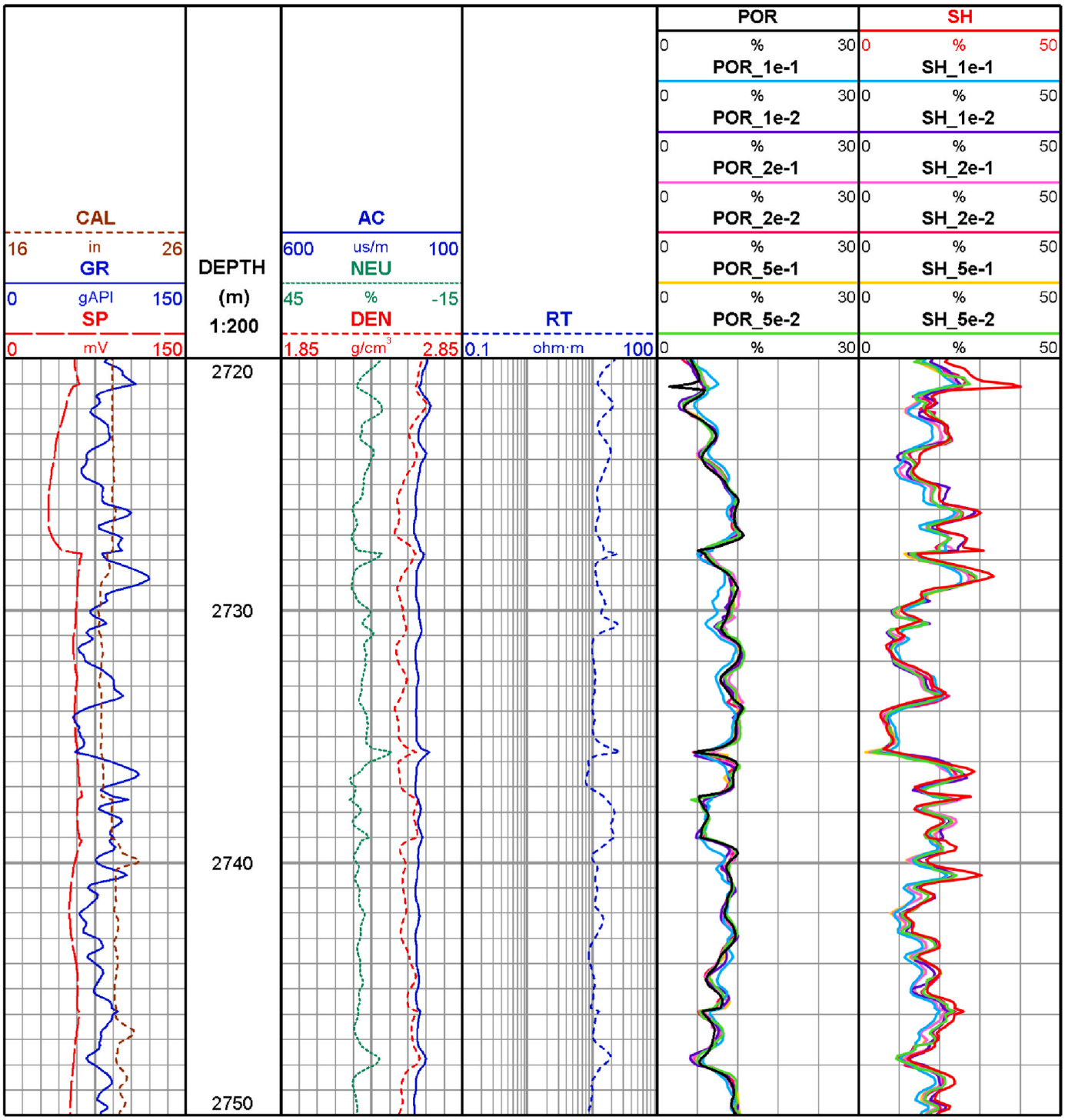


**Fig. 10.** Comparison of actual application performance of petrophysical constraint model with different ε. POR/SH_1e-2, POR/SH_2e-2, POR/SH_5e-2, POR/SH_1e-1, POR/SH_2e-1, and POR/SH_5e-1 represent taking ε as 0.01, 0.02, 0.05, 0.1, 0.2,0.5 respectively.

the gamma ray logging response function used in the petrophysical constraint, we set $\lambda_{PI} = 0.1$ and $\varepsilon = 0.05$.

The indicators to evaluate model are the same as in section 2.1.3. Table 4 lists the performance of various models in the test set.

The data quality of the 2021 SPWLA PDDA dataset is better than that of the field data in section 3.1, and the data-driven machine learning models perform better. The petrophysical informed model and transfer learning methods both improve the model performance, as observed in section 3.1.3. The PI_DNN_b model performs better than the DNN_b model, whit a more than 2 % lower MAPE_AVG and an improvement in the prediction performance of shale volumetric concentration, where the MAPE decreases by about 5.5 %. The PI_ResNN_b model shows a decrease in MAPE_AVG of about 3.5 % compared with that of the ResNN_b model, with the porosity prediction performance improving most notably, with a decrease in MAPE of about 4.5 %. The transfer learning model trained by the fine-tuning is better than that trained by freezing, while the prediction performance of porosity and water saturation in DNN_target_ft_b is worse than that in PI_DNN_b. The same is observed for the ResNN_target_ft_b model, where the prediction performance of porosity and water saturation is inferior to that in

**Table 7**
Experimental results of noise resistance of the pure data-driven residual neural network model (ResNN) and the petrophysical informed residual neural network model (PI-ResNN).

| | model | Out-put | MAPE_AVG | MAPE | MAE | MSE ± std |
|---|---|---|---|---|---|---|
| 10 | ResNN | SH | 12.94 | 16.88 | 2.74 | 17.86 ± 4.0 |
| | | POR | | 9.00 | 0.81 | 1.12 ± 1.02 |
| | PI-ResNN | SH | 11.59 | 16.15 | 2.53 | 15.45 ± 3.9 |
| | | POR | | 7.03 | 0.63 | 0.78 ± 0.88 |
| 20 | ResNN | SH | 15.51 | 18.06 | 2.97 | 17.62 ± 2.9 |
| | | POR | | 12.95 | 1.15 | 2.22 ± 1.45 |
| | PI-ResNN | SH | 12.96 | 16.84 | 2.60 | 14.80 ± 3.8 |
| | | POR | | 9.08 | 0.83 | 1.18 ± 1.02 |
| 30 | ResNN | SH | 17.05 | 20.76 | 3.51 | 23.18 ± 4.2 |
| | | POR | | 13.34 | 1.21 | 2.51 ± 1.50 |
| | PI-ResNN | SH | 15.27 | 19.49 | 3.17 | 19.63 ± 4.0 |
| | | POR | | 11.09 | 1.06 | 1.68 ± 1.03 |
| 40 | ResNN | SH | 19.06 | 21.53 | 3.72 | 26.45 ± 4.4 |
| | | POR | | 16.58 | 1.62 | 3.87 ± 1.51 |
| | PI-ResNN | SH | 16.29 | 18.82 | 3.22 | 20.77 ± 4.0 |
| | | POR | | 14.03 | 1.35 | 2.79 ± 1.32 |
| 50 | ResNN | SH | 20.10 | 28.77 | 5.11 | 42.15 ± 4.5 |
| | | POR | | 21.42 | 2.14 | 6.73 ± 1.84 |
| | PI-ResNN | SH | 21.47 | 23.23 | 4.21 | 31.37 ± 4.2 |
| | | POR | | 19.71 | 1.97 | 5.44 ± 1.50 |

PI_ResNN_b.

Compared with field data in section 3.1, the 2021 SPWLA PDDA competition data is more sensitive to the petrophysical constraint. The experimental results show that the structure of the ResNN is more suitable for adding petrophysical constraints. Fig. 8 shows the application of a well in the test set of all models trained on the 2021 SPWLA PDDA competition data.

## 4. Influence of mechanism model on the petrophysical informed model

In this section, we will discuss the effect of the two parameters ($\lambda_{PI}$ and $\varepsilon$) on the performance of the petrophysical informed model and test its anti-noise performance based on the measured data in an oilfield in China. Many petrophysical logging response functions are the empirical formula, which is not accurate and cannot apply to all situations. It is critical to control the fusion degree of the mechanism model in the petrophysical informed model. We hope that the empirical formula can optimize model the model quickly and explore a more accurate mapping relationship between input and output data.

We use the multi-task ResNN with two outputs (porosity and shale volumetric concentration) as the basic model. All models take the parameters of the pre-training model (100 epochs of data-driven training) as initial parameters to avoid the uncertainty of parameter updates caused by random parameter initialization. The selection of the total loss function and other model optimization methods are the same as those in section 3.1.

### 4.1. Weight of petrophysical constraints

The weight of petrophysical petrophysical constraint $\lambda_{PI}$ can control the proportion of the petrophysical constraint in the total loss function. The larger the $\lambda_{PI}$, the more significant the influence of petrophysical information on the model. As the logging response function is a simplification of the real situation and the downhole formation is uncertain and heterogeneous, the logging response function may not be reliable, and the $\lambda_{PI}$ needs to be tested to find a suitable value. We set $\lambda_{PI}$ as 0, 0.01, 0.02, 0.05, 0.1, 0.2, and 0.5, and set $\varepsilon$ as 0.1 to test the model's performance on the test set after 10,000 epochs of training under different weights of petrophysical constraints (shown in Table 5).

The experimental results show that $\lambda_{PI}$ affects the petrophysical informed model's performance. If $\lambda_{PI}$ is too large or too small, the petrophysical informed model cannot achieve the best performance. Specifically, the MAPE_AVG of the model first decreases and then increases with the increase of $\lambda_{PI}$. When $\lambda_{PI} = 0.1$, the performance of shale volumetric concentration is the best, and when $\lambda_{PI} = 0.05$, the performance of porosity is the best, and the model's MAPE_AVG is the lowest. If the $\lambda_{PI}$ is too small, the mechanism model cannot compete with the data-driven model, and the fusion between data-driven and mechanism models cannot be achieved. If the $\lambda_{PI}$ is too large, the petrophysical informed model cannot extract information from the data, and the prediction performance may decrease due to the mismatch between the mechanism and the data-driven models.

Currently, there is no suitable method for selecting $\lambda_{PI}$, and it needs constant adjustment according to data quality, mechanism model accuracy, and neural network structure. Overall, if the mechanism model is accurate or the data quality is low, we can set $\lambda_{PI}$ to a large value. If the reliability of the mechanism model is not good, the $\lambda_{PI}$ should be set to a small value. Fig. 9 shows the comparison of prediction performances of different $\lambda_{PI}$ on the test set.

### 4.2. Allowable error of petrophysical constraints

The $\lambda_{PI}$ adjusts the proportion of the petrophysical constraint in the total loss function, thus affecting response functions in the petrophysical informed model. While the allowable error $\varepsilon$ sets a "buffer zone" for the petrophysical informed model, and adjusts the fusion degree according to the accuracy of the mechanism model.

In the case of Eq. (22) as the total loss function, we set $\lambda_{PI} = 0.1$ and $\varepsilon$ as 0.01, 0.02, 0.05, 0.1, 0.2 and 0.5 respectively, representing the allowable error of the gamma ray logging response function of 1 %, 2 %, 5 %, 10 %, 20 % and 50 %. The performance of models with different $\varepsilon$ on the test set after 10,000 epochs of training is shown in Table 6.

As the $\varepsilon$ increases, the MAPE_AVG of the model first decreases and then increases. The optimal model performance is achieved when $\varepsilon = 0.05$. Compared to the result in section 4.1, the variation of $\varepsilon$ has less impact on the model performance. While the gamma ray logging response function is mainly influenced by shale volumetric concentration, the prediction performance of shale volumetric concentration has a less noticeable differences. However, the variation in the porosity prediction performance is relatively obvious, with the difference of over 2 % between the lowest MAPE ($\varepsilon = 0.1$) and the highest MAPE ($\varepsilon = 0.01$), and a prediction performance improvement of about 24 %.

The $\varepsilon$ can be a double-edged sword for the petrophysical informed model. It can reduce the influence of inaccurate mechanism models on neural networks and leave a buffer for the fusion of mechanism model and data-driven model. However, if the accuracy of the mechanism model is high, the error of the mechanism model and output value may be always within the error tolerance range, and the petrophysical constraint fails to play an auxiliary role in model training.

In general, the $\varepsilon$ is only related to the precision of the mechanism model, and the higher the precision, the lower $\varepsilon$. In logging reservoir parameter prediction, $\varepsilon$ can be evaluated by referring to the measurement error calculation of logging response functions when fusing logging response functions with data-driven model. Fig. 10 shows the comparison of prediction performances of different $\varepsilon$ on the test set.

### 4.3. Noise resistance

Previous research shows that the data-mechanism-driven model exhibits strong robustness and anti-noise performance. In this section, we test the petrophysical informed model and pure data-driven model on noisy data to verify the anti-noise performance. We add the noise of 10 %, 20 %, 30 %, 40 %, and 50 %, respectively, to the original data as the labels in training data, with noise following a normal distribution, where the mathematical expectation is 0 and variance is (Noise*mean(SH))2 or (Noise*mean(POR))2. The test data are noise-free. We set $\lambda_{PI} = 0.1$, $\varepsilon = 0.1$, and use different proportions of noisy labels to train the pure data-

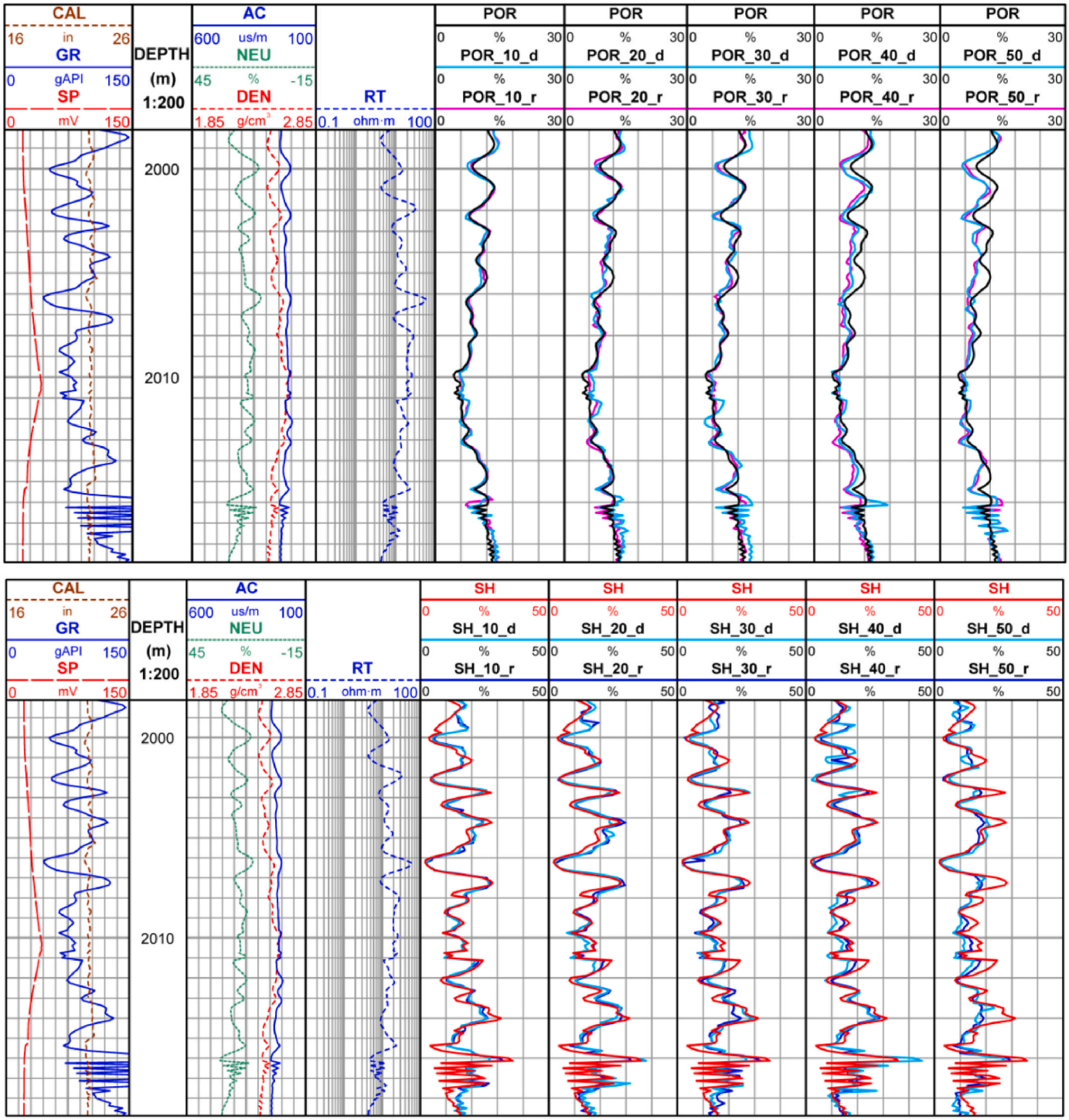


**Fig. 11.** Comparison of the actual application performance of the model with petrophysical constraint on noise resistance. POR and SH are the corresponding labeled reservoir parameters without adding noise. The number in the suffix of reservoir parameters is the noise addition ratio, 'd' is the pure data-driven model, and 'r' is the model with the petrophysical constraint. **(a)** is the comparison of porosity (POR) prediction performance, and **(b)** is the comparison of shale volumetric concentration (SH) prediction performance.

driven model and the petrophysical informed model. Table 7 shows the performance of each model on the test set without noise.

According to the experiments, PI-ResNN exhibits good anti-noise performance. The MAPEs of shale volumetric concentration and porosity in five groups of noisy data are lower than that in the ResNN model. If there is 10 % noise, the MAPE_SUM of the PI-ResNN model decreases by 1.4 % compared to that of the ResNN model, and the prediction performance increases by 10.43 %. If there is 20 % noise, MAPE_SUM decreases by 2.5 %, and the prediction performance increases by 16.41 %. If there is 30 % noise, MAPE_SUM decreases by 1.8 %, and the prediction performance increases by 10.32 %. If there is 40 % noise, MAPE_SUM decreases by 2.6 %, and the prediction performance increases by 13.80 %. If there is 50 % noise, MAPE_SUM decreases by 3.6 %, and the prediction performance increases by 14.45 %.

As the noise increases, we can adjust $\lambda_{PI}$ appropriately to achieve better performance. However, in this control experiment, the model

parameters are fixed, and $\lambda_{PI}$ are not allowed to adjust. Theoretically, the noise resistance performance of PI-ResNN is better than that of the experiment if we increase $\lambda_{PI}$ with noise growth. Fig. 11 shows the effect comparison of the model with and without petrophysical constraints on the test set.

## 5. Conclusions

In this paper, we present a construction method for the data-mechanism-driven reservoir evaluation model and introduce a "petrophysical constraint neural network" for reservoir evaluation. In comparison to transfer learning, the petrophysical constraint selectively adds the petrophysical mechanism model to the data-driven model. The petrophysical constraint fuses the data-driven and mechanism models to improve the generalization of the neural network model and the accuracy and stability of inversion results. The advantages and application performances of the petrophysical constraint are verified by the case studies, and two parameters affecting the effect of mechanism model addition are tested. The following conclusions can be drawn:

1) Data quality is the key factor that affects the performance of the model. For machine learning, selecting the dataset is more important than choosing the model structure. Therefore, the construction of high-quality petrophysical logs dataset is an important foundation for the development of the intelligent interpretation method.
2) Both transfer learning and petrophysical constraint can improve the prediction performance. However, the application of petrophysical constraint to the mechanism model is more clear.
3) Mechanism-driven participation in model training does not always improve model performance. The weight of the petrophysical constraint should be adjusted according to the data quality and accuracy of the mechanism model. An appropriate allowable error should be set based on the systematic error of the mechanism model.
4) The addition of petrophysical constraint can improve the noise resistance of the model and its adaptability to low-quality data to a certain extent.
5) The residual neural network is more sensitive to the petrophysical constraint. The short-cut layer retains more information in the original input data, and future research on the petrophysical constraint can be carried out based on the residual neural network.

Although the petrophysical constraint can improve the performance of the reservoir evaluation model, the improvement is not as significant compared to transfer learning. Furthermore, since the petrophysical mechanism model is fixed during model training, it is necessary to select the petrophysical mechanism model carefully and corresponding parameters should be tested to ensure the good performance of petrophysical constraint. In the future, the selection of parameters in different fields and geological characteristics can be studied to improve the adaptability of this method. In addition, it should be noted that data quality is also an important factor that affects AI models. We are currently building a high-quality logging public dataset, which contains actualmeasured and synthetic logging data of different regions, different strata, different lithologies, and different physical properties. It will further facilitate the development of AI algorithms in the field of geophysical logging.

## CRediT authorship contribution statement

**Rongbo Shao:** Methodology, Software, Writing – original draft, Writing – review & editing. **Hua Wang:** Validation, Writing – review & editing. **Lizhi Xiao:** Methodology, Supervision, Writing – review & editing, Funding acquisition.

## Declaration of competing interest

The authors declare that they have no known competing financial interests or personal relationships that could have appeared to influence the work reported in this paper.

## Acknowledgments

This work was supported by the Strategic Cooperation Technology Projects of CNPC and CUPB (ZLZX2020-03), National Key Research and Development Program (2019YFA0708301), National Key Research and Development Program (2023YFF0714102), Science and Technology Innovation Fund of CNPC (2021DQ02-0403). Thanks for reviewers' opinions, these comments are very helpful to improve the quality of the manuscript.

## References

Abdulraheem, A., Sabakhy, E., Ahmed, M., Vantala, A., Korvin, G., 2007. Estimation of Permeability from Wireline Logs in a Middle Eastern Carbonate Reservoir Using Fuzzy Logic. Society of Petroleum Engineers.
Adoghe, L.I., Aniekwe, O.S., Nwosu, C., 2011. Improving Electrofacies Modeling Using Multivariate Analysis Techniques: A Deepwater Turbidite Case Study.
Bergen, K., Johnson, P., Hoop, M., et al., 2019. Machine learning for data-driven discovery in solid Earth geoscience. Science 363 (6433), eaau0323.
Chen, Y., Zhang, D., 2020. Physics-constrained deep learning of geomechanical logs. IEEE Trans. Geosci. Rem. Sens. 58 (8), 5932–5943.
Chen, Y., Zhang, D., 2021. Theory-guided deep-learning for electrical load forecasting (TgDLF) via ensemble long short-term memory. Advances in Applied Energy 1, 100004.
Chen, Y., Huang, D., Zhang, D., Zeng, J., Wang, N., Zhang, H., Yan, J., 2021. Theory-guided hard constraint projection (HCP): a knowledge-based data-driven scientific machine learning method. J. Comput. Phys. 445, 110624.
Chen, M., Wang, H., 2022. Explainable machine learning model for predication of ground motion parameters with uncertainty quantification. Chin. J. Geophys. 65 (9), 3386–3404 (in Chinese with English Abstract).
Goodfellow, I., Bengio, Y., Courville, A., 2016. Deep Learning. MIT Press.
He, K., Zhang, X., Ren, S., Sun, J., 2016. Deep residual learning for image recognition. In: Proceedings of the IEEE Conference on Computer Vision and Pattern Recognition, pp. 770–778.
Jaikla, C., Devarakota, P., Auchter, N., et al., 2019. FaciesNet: machine learning applications for facies classification in well logs. In: Machine Learning and the Physical Sciences Workshop at the 33rd Conference on Neural Information Processing Systems (NeurIPS). Vancouver, Canada.
Karpatne, A., Atluri, G., Faghmous, J.H., Steinbach, M., Banerjee, A., Ganguly, A., Kumar, V., 2017a. Theory-guided data science: a new paradigm for scientific discovery from data. IEEE Trans. Knowl. Data Eng. 29 (10), 2318–2331.
Karpatne, A., Watkins, W., Read, J., Kumar, V., 2017b. Physics-guided Neural Networks (Pgnn): an Application in Lake Temperature Modeling arXiv preprint arXiv: 1710.11431, 2.
Kharazmi, E., Zhang, Z., Karniadakis, G.E., 2019. Variational Physics-Informed Neural Networks for Solving Partial Differential Equations arXiv preprint arXiv:1912.00873.
Kharazmi, E., Zhang, Z., Karniadakis, G.E., 2021. hp-VPINNs: Variational physics-informed neural networks with domain decomposition. Comput. Methods Appl. Mech. Eng. 374, 113547.
Kingma, D., Ba, J., 2014. Adam: a method for stochastic optimization. Computer Science arXiv:1412.6980.
Lacentre, P., Carrica, P., 2003. A Method to Estimate Permeability on Uncored Wells Based on Well Logs and Core Data. Spe Latin American & Caribbean Petroleum Engineering Conference.
Lee, S.H., Dattagupta, A., 1999. Electrofacies characterization and permeability predictions in carbonate reservoirs: role of multivariate analysis and nonparametric regression. In: Proceedings - SPE Annual Technical Conference and Exhibition.
Liu, X., Zhou, L., Chen, X., et al., 2020. Lithofacies identification using support vector machine based on local deep multi-kernel learning. Petrol. Sci. 17, 954–966. https://doi.org/10.1007/s12182-020-00474-6.
Male, F., Jensen, J.L., Lake, L.W., 2020. Comparison of Permeability Predictions on Cemented Sandstones with Physics-Based and Machine Learning Approaches. Earth Arxiv.
Michael, A.N., 2015. Neural Networks and Deep Learning. Determination Press.
Raissi, M., Karniadakis, G.E., 2018. Hidden physics models: machine learning of nonlinear partial, differential equations. J. Comput. Phys. 357, 125–141.
Raissi, M., Perdikaris, P., Karniadakis, G.E., 2019. Physics-informed neural networks: a deep learning framework for solving forward and inverse problems involving nonlinear partial differential equations. J. Comput. Phys. 378, 686–707.
Shao, R., Xiao, L., Liao, G., et al., 2022. A reservoir parameters prediction method for geophysical logs based on transfer learning. Chin. J. Geophys. 65 (2), 796–808. https://doi.org/10.6038/cjg2022P0057 (in Chinese).
SPWLA, 2021. SPWLA PDDA Machine Learning Competition, p. 2021. https://github.com/pddasig/Machine-Learning-Competition-2021#well-log-based-reservoir-property-estimation-with-machine-learning.

Wang, H., Wu, Y., Zhang, Y., Lai, F., 2023. Uncertainty and explainable analysis of machine learning model for reconstruction of sonic slowness logs. Artif. Intell. Geosci. 4, 182–198 (2023).
Wang, H., Zhang, Y., 2021. Research status and prospect of artificial intelligence in logging data processing and interpretation. Well Logging Technol. 45 (4), 345–356. Chinese with English abstract.
Wang, N., Chang, H., Zhang, D., 2020a. DeepLearning-based inverse modeling approaches: a subsurface flow. J. Geophys. Res. Solid Earth, e2020JB020549.
Wang, N.H., Zhang, D., 2021. Efficient uncertainty quantification for dynamic subsurface flow with surrogate by Theory-guided Neural Network. Comput. Methods Appl. Mech. Eng. 373, 113492.
Wang, N., Zhang, D., Chang, H., Li, H., 2020b. Deep learning of subsurface flow via theory-guided neural network. J. Hydrol. 584, 124700.
Xiao, L., 2022. The fusion of data-driven machine learning with mechanism models and interpretability issues. Geophys. Prospect. Pet. 61 (2), 205–212.
Xu, R., Zhang, D., Rong, M., Wang, N., 2021. Weak form theory-guided neural network (TgNN-wf) for deep learning of subsurface single- and two-phase flow. J. Comput. Phys. 436, 110318.
Zhu, Y., Zabaras, N., 2018. Bayesian deep convolutional encoder-decoder networks for surrogate modeling and uncertainty quantification. J. Comput. Phys. 366, 415–447.